

Intriguing CeO₂-TiO₂ hybrid nanostructured photoanode resulting up to 46% efficiency enhancement for dye-sensitized solar cells

Anurag Roy,* Shubhranshu Bhandari, Senthilarasu Sundaram, Tapas K. Mallick

Environment and Sustainability Institute, University of Exeter, Penryn Campus, Cornwall TR10 9FE, UK.

*Email: A.Roy30@exeter.ac.uk; ar.chem30@gmail.com

ABSTRACT

The harvesting of electrical energy from sunrays with low cost, clean form and prosperity is an excellent progression. In this context, significant advancement has been made in the solar energy area in terms of cell's design to enhance efficiency. Light scattering may benefit solar cells in this aspect by extending the travelling distance of light within the photoelectrode film. In this work, dextran templating high-surface-area contained CeO₂ nanoparticles (~22 nm) were employed to improve the power conversion efficiency (PCE) of a TiO₂-based dye-sensitized solar cell (DSSCs). Various physicochemical techniques were investigated to characterize the synthesized CeO₂ nanoparticles. Synthesized cubic CeO₂ nanoparticles were further explored as an additional layer on the top of the synthesized anatase TiO₂ nanocube based film to fabricate CeO₂-TiO₂ hybrid photoanode, encouraging light scattering in DSSCs. A comparative study was undertaken to understand the effect of the CeO₂ layer on the synthesized and standard anatase TiO₂. The overall power conversion efficiency obtained for hybrid photoanode-based DSSC is 8.92%, ~46% higher than that of TiO₂ nanocubes-based photoanode, a considerably improved open-circuit voltage of 0.83V under 1 SUN 1.5 AM. In addition, the PCE enhancement is observed only ~8% using standard TiO₂ based photoanode under the same condition. The photovoltaic performance highlights that dextran templating CeO₂ nanoparticle exhibits a significant impact as the light scattering layer and heterojunction formation when incorporating on top of the anatase TiO₂ nanocube resulting in a hybrid photoanode enhancing the PCE of DSSCs. This alternative approach could facilitate the performance of TiO₂ based DSSCs towards improving efficiency.

Keywords: CeO₂, light scattering, optoelectronic materials, photovoltaic, heterojunction

1. Introduction

As a typical renewable energy source, solar energy is an ideal alternative to traditional conventional energies due to its low cost, green, inexhaustible, not limited to a region and environmentally friendly behaviour [1]. Initiating with the first generation of solar cells, extensive research works have produced significant achievements in the solar energy field, which led to developing the various third-generation solar cells [2–4]. As one of the oldest among the emerging photovoltaics (PV) technologies, dye-sensitized solar cells (DSSCs) have opened new energy prospects due to their lower cost and more accessible fabrication perspective, achieving the highest power conversion efficiency (PCE) of 13% to date [5,6]. With the development of new nanostructured materials, synthesis technologies, refinement processes, the field of DSSC is also improving day by day [7–10]. The essence of DSSC consists of a sandwich-type photoelectrochemical cell invented with two electrodes and an electrolyte in operation by light-induced redox reactions [11,12]. Strategies like ion doping, decoration of noble metals, refinement with metal oxides, modifications with up/down conversion materials, development of different dyes, using various electrolytes and investigation of varying counter electrodes including carbon-based materials, composites and polymers, have assisted the DSSC to the next level [13,14]. Traditionally, TiO_2 is the most vital component of DSSC, which promises high PCE and stability [15]. However, due to the limitation of physicochemical properties, TiO_2 photoanode often shows discouraging efficiency improvement [16]. In this stage, searching for a better strategy, which can facilitate the performance of TiO_2 , is highly essential [17]. However, it is a challenge to improve further the performance of TiO_2 by the utilization of tailored geometries. TiO_2 is majorly consisted of thermodynamically stable anatase or rutile phase and synthesized in several morphological forms [18]. Various studies have been

carried out with anatase and rutile regular phases of TiO₂, leading to noticeable outcomes of DSSC applications, although the traditional electrodes composed of nanometer-sized TiO₂ particles sufferers insufficient electron diffusion coefficient limiting the PCE [19–21]. In this context, different methods have been attempted to incorporate suitable modifications into conventional TiO₂ photoanode by enlarging the light-harvesting, reducing recombination, and promoting electron transfer rate [22]. Besides, allowing effective separation, lowering electron recombination, and collecting energy-bearing photocarriers are vital for the DSSCs operation, which various nanointerfaces can tailor in DSSCs [23,24]. The synergistic effects of the three major factors, such as light scattering, electron transfer efficiency, and dye adsorption, influence the current density (J_{SC}) and exhibit the maximum value in enhancing PCE [25,26]. In this respect, the introduction of an optical scattering layer considered one of the most innovative strategies to improve the photoanode's light-harvesting capability [16,27]. More efficient light scattering materials and adequate light scattering structures are still in need with the planar scattering effect. In recent years, several light scattering layers based on TiO₂, ZnO, SnO₂, CuO, W₂O₃, BaTiO₃, reduced graphene oxides, graphene quantum dots, carbon nanotubes etc. have been utilized to boost up the performance of DSSCs [28]. Among different oxides, cerium dioxide (CeO₂) has already proved its efficacy in fuel cell electrolytes, gas sensors, ultraviolet absorbers for sunscreens, and others, influencing the researchers to reveal its applicability in DSSC [29]. The CeO₂ based scattering approach on the efficiency improvement of DSSCs was initially implemented by Yu et al. (2012) by utilizing the mirror-like light scattering effect of CeO₂, which produced a noticeable PCE improvement of 17.8% in the case of a TiO₂ based DSSC [30]. Recently, a hybrid double-shell CeO₂@TiO₂ hollow sphere exhibited 7.95% PCE reported by Bai et al. (2017) [31]. At the same time, Han et al. (2017) reported 7.05% PCE with

an enhancement of 27% using Er, Yb-CeO₂ hollow spheres as a scattering layer [32]. Song et al. (2016) reported the overall efficiency of 9.86% obtained by atomic layer deposited TiO₂ photoanode modified with flower-like CeO₂ scattering layer, which is 31% higher than that of the conventional TiO₂ photoanode [33]. CeO₂ can take different shapes and sizes depending on the synthesis methods. Typically, a cubic nanostructure has long been considered a valuable material for high-refractive index film in single and multi-layer optical coatings [34–36]. Therefore, the implementation of cubic CeO₂ as a light scattering layer on the top of the TiO₂ layer to form a bi-layered photoanode are expected to be a potential alternative to achieve more efficient light-harvesting for benefiting DSSCs performance. Both a high surface area and good light scattering are the two major factors influencing light harvesting. Herein, we introduce a cubic CeO₂ nanoparticles layer onto the top of a hydrothermally synthesized TiO₂ (nanocubes) layer to fabricate a hybrid CeO₂-TiO₂ photoanode for DSSCs application. Also, this experiment reveals the combined effect of the scattering layer's thickness and TiO₂ nanocube based photoanode with a detailed explanation. Furthermore, we have compared the effect of CeO₂ layer with the commercial and synthesized TiO₂ photoanodes to understand the maximum efficiency generation. Our observation suggests an increase in the CeO₂ layer thickness enhances the diffused reflectivity in the photoanodes while suppressing the photoanode's dye-loading capacity, reducing the performance of the device. In this work, we have observed a massive efficiency enhancement ~46% predoming from the short-circuit current and open circuit voltage for the synthesized TiO₂-based photoanode when employing a layer of CeO₂ on the top of the device. We believe the recorded efficiency enhancement is quite competitive among the recent related studies.

2. Materials and Methods

2.1. Synthesis of TiO₂ Nanocube

Synthesis of TiO₂ nanocubes was adopted from work reported by Mukhopadhyay et al. (2016) [37]. In short, titanium (IV) isopropoxide (TTIP, C₁₂H₂₈O₄Ti, Sigma Aldrich) was mixed with triethanolamine (TEOA, C₆H₁₅NO₃, Merck) at a molar ratio of TTIP/TEOA = 1:2, and 0.02 mol dm⁻³ of Na-oleate under constant stirring (pH ~ 10 ± 0.5). After that, the resulting mixture was transferred to a closed flask and kept undisturbed for 24 h at 100 °C to form gelation. Next, the viscous gel was shifted to a Teflon-lined autoclave and aged at 140 °C for 72 h to nucleate and grow the TiO₂ particles. Finally, the product was washed with distilled water several times to reduce the pH of < 8 and finally dried under a vacuum at 120 °C for further use.

2.2. Synthesis of CeO₂ Nanoparticles

CeO₂ nanoparticles were synthesized using a 50 mL aqueous solution containing 0.274g of Cerium Nitrate, Ce(NO₃)₃. 6H₂O (Alfa Aesar, Ward Hill, MA) and 2 g of dextran, H(C₆H₁₀O₅)_xOH (Alfa Aesar, Ward Hill, MA). The solution was vigorously stirred for 30 minutes to get a transparent homogeneous sol by ageing for 18 h to form a gel. Further, the gel was preheated to 100°C followed by direct calcination at 500°C for 2h to produce CeO₂ nanoparticles. Dextran mediated synthesis has many benefits like high water-soluble glucose-based polysaccharides, less stringent use conditions, consisting of unique structural engagement with multiband orientation suitable as a soft sacrificial templating agent to synthesize discreet homogeneous nanostructured.

3. Material Characterization

X-ray diffraction (XRD) measurements of TiO₂ nanocubes and CeO₂ nanoparticles were carried out using X'pert pro MPD XRD of PANalytical system with CuK_α radiation ($\lambda = 1.5406 \text{ \AA}$). Besides, the Fourier transformed-infrared (FTIR) spectrum of CeO₂ nanoparticles was performed on a Perkin Elmer, Spectrum two FT-IR spectrometer. The bright-field image, high-resolution transmission electron microscopy image (HRTEM) of TiO₂ nanocubes and CeO₂ nanoparticles was explored using Tecnai G2 30ST (FEI), 300 kV. The Raman spectrum of CeO₂ nanoparticles was measured using the Raman spectrophotometer STR500 (Cornes Technologies system using 514.5nm Ar⁺ green laser with 50mW power). Field emission scanning electron microscope (FESEM) of CeO₂-TiO₂ hybrid photoanode was executed utilising a TESCAN VEGA3 SEM. The specific surface area of CeO₂ nanoparticles was measured by using Quantachrome (iQ3) instrument. Brunauer-Emmett-Teller (BET) theory was applied to calculate the specific surface area of the CeO₂ nanoparticle. Besides, the corresponding pore size distribution was evaluated from Barrett, Joyner, and Halenda (BJH) method. The UV-Vis-NIR spectrophotometer's absorption spectra and diffused reflectance spectrum of CeO₂ nanoparticles were carried out (SHIMADZU UV-3600). The photoluminescence spectra were recorded on a spectro-fluorimeter (QM-40, Photon Technology International, PTI). X-ray photoemission spectroscopy (XPS) measurements of CeO₂ nanoparticle was executed in a PHI 5000 Versa probe II scanning XPS microprobe (ULVAC-PHI, US).

4. Fabrication of DSSC

Pieces with a size of $2 \times 2 \text{ cm}^2$ of transparent conducting oxide [fluorine-doped tin oxide (FTO)] glass substrates having the sheet resistance of $8 \text{ } \Omega/\text{cm}^2$ were first ultrasonicated in deionized

water and ethanol. Next, they were subjected to surface cleaning by using a UV-Ozone cleaner (Ossila UV Ozone Cleaner, UK) for 15 min to remove any dirt, patches on the surface of the FTO glasses. Meantime, the synthesized TiO_2 samples were employed for the paste preparation with ethyl cellulose (Merck, U.K) in a proportion of 2:1 with a periodic drop of 5 ml of α -Terpineol (Merck, UK). We used two layers of TiO_2 paste (ST) to fabricate the photoanode using the screen printing (120T mesh/inch, Mascoprint, UK) method followed by annealing under an ambient atmosphere following multiple heating steps (125 °C for 5 min, 375 °C for 10 min and 450 °C for 30 min.) on a hot plate. The film thickness of the TiO_2 layer was maintained at $\sim 6 \mu\text{m}$ while using the screen-printing process. The synthesized CeO_2 sample also underwent a similar paste preparation method as mentioned above. CeO_2 was deposited as a next layer on the top of the deposited TiO_2 layers and further followed the similar fabrication process as described above.

Similarly, a layer of 20 nm commercial TiO_2 pastes from Greatcell Solar, such as 18NR-T and 18NR-AO, was coated on the FTO glass by the screen printing method (CT). The CeO_2 was introduced, such as one layer (C1) and two layers (C2) on the top of both types of TiO_2 films to fabricate the hybrid films. The final active area was selected as 0.2826 cm^2 for the solar cell testing purpose. An ethanolic solution of N719 dye (0.5 mM, Solaronix) was used for the dye sensitization. The films were soaked inside the dye solution for 24h. Then, the dye-adsorbed CeO_2 - TiO_2 (STC and CTC) hybrid film and a platinized FTO substrate were placed like a sandwich in the presence of prepared I_3^-/I^- liquid electrolyte to make a DSSC device. The process as mentioned above has been followed to make ST and CT-based DSSCs. Finally, the device was allowed to test under 1000 W/m^2 using the Wacom AAA continuous solar simulator [38]. Six

sets of devices have been used for their photovoltaic performances, and the champion cell' data is reported.

5. Results and Discussions

5.1 Structural and Optical Analysis of TiO₂ Nanocubes

As mentioned in our earlier report, we have used the same anatase TiO₂ nanocubes [37]. The X-ray diffraction (XRD) patterns of synthesized TiO₂ nanocubes reflected well-resolved significant diffraction peaks corresponding to the anatase TiO₂ phase, which matches well with the reported standard XRD pattern in the JCPDS card number 21-1272, as shown in **Fig. 1a**. The TEM bright-field images confirm the crystalline nature of the cube shape of the synthesized TiO₂, as shown in **Fig. 1b**. The distinct lattice fringes in the high-resolution TEM image (inset of **Fig. 1b**) corresponds to the (101) reflection with a lattice spacing of 3.51 Å and further confirms the high anatase phase of the sample. Highly crystalline TiO₂ nanocubes were synthesized in purely anatase crystalline form, having an average crystallite size of 21 nm.

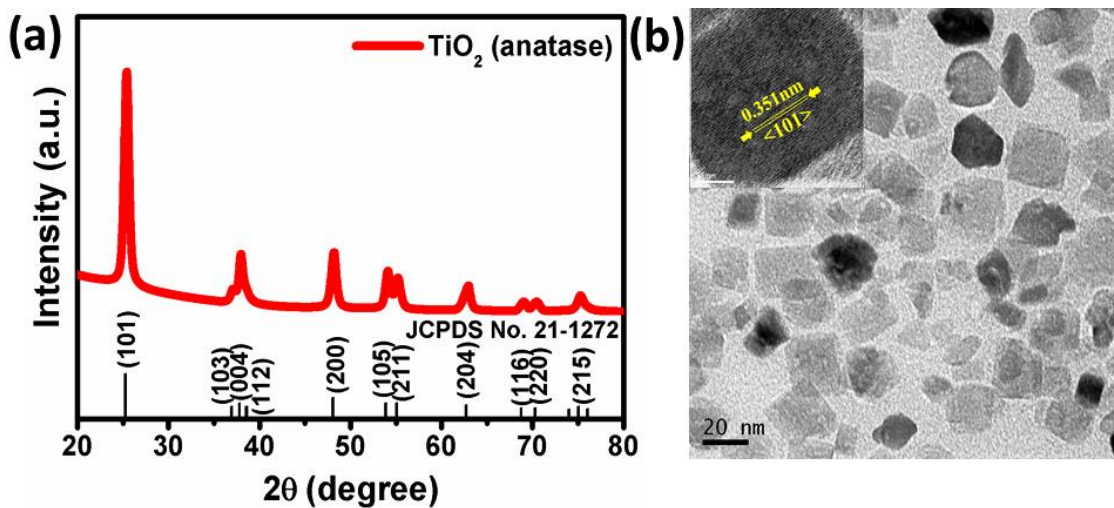


Fig. 1. (a) X-ray diffraction pattern with standard JCPDS card no. 21-1272 and (b) TEM bright-field image of the hydrothermally synthesized TiO₂ sample (inset: corresponding HRTEM image).

5.2 Structural and Optical Analysis of CeO₂

The X-ray diffraction pattern shown in **Fig. 2a** reveals a polycrystalline cubic CeO₂ structure as it matches well with the reference diffraction pattern of CeO₂ (JCPDS card number 81-0792) [39]. The calculated lattice parameter was observed to 5.411 Å. According to the Debye-Scherrer formula, the strongest reflections (111) at $2\theta=28.56^\circ$ was used to calculate the average crystallite size of the CeO₂ nanoparticles, which was determined to be around ~20 nm. The FTIR spectrum of the obtained CeO₂ nanoparticles is shown in **Fig. 2b**. The absorption band that appeared at wavenumber 622 cm⁻¹ represents the Ce-O stretching band. Besides, the prominent band at 3410 cm⁻¹ indicates the stretching band of the hydroxyl group end. At the same time, the stretching band appearing at 1633 and 1448 cm⁻¹ signify anti-symmetric and symmetric vibration of the carboxyl [40]. CeO₂ consists Ce-O-Ce symmetric vibration in their fluorite type crystal structure, which allows T_{2g} Raman mode. In the present study, the significant Raman band observed at ~460 cm⁻¹ (**Fig. 2c**) is assigned to the first-order scattering [41]. The absorption spectrum of CeO₂ in the spectral range of 200-800 nm is presented in **Fig. 2d**. A broad distinct peak has been observed at ~430 nm, which indicates the distinct formation of CeO₂. The optical bandgap (E_g) was estimated using the Tauc plot formula and is found ~3.02 eV, indicates reduced particle size formation of CeO₂, as shown in **Fig. 2d (inset)**.

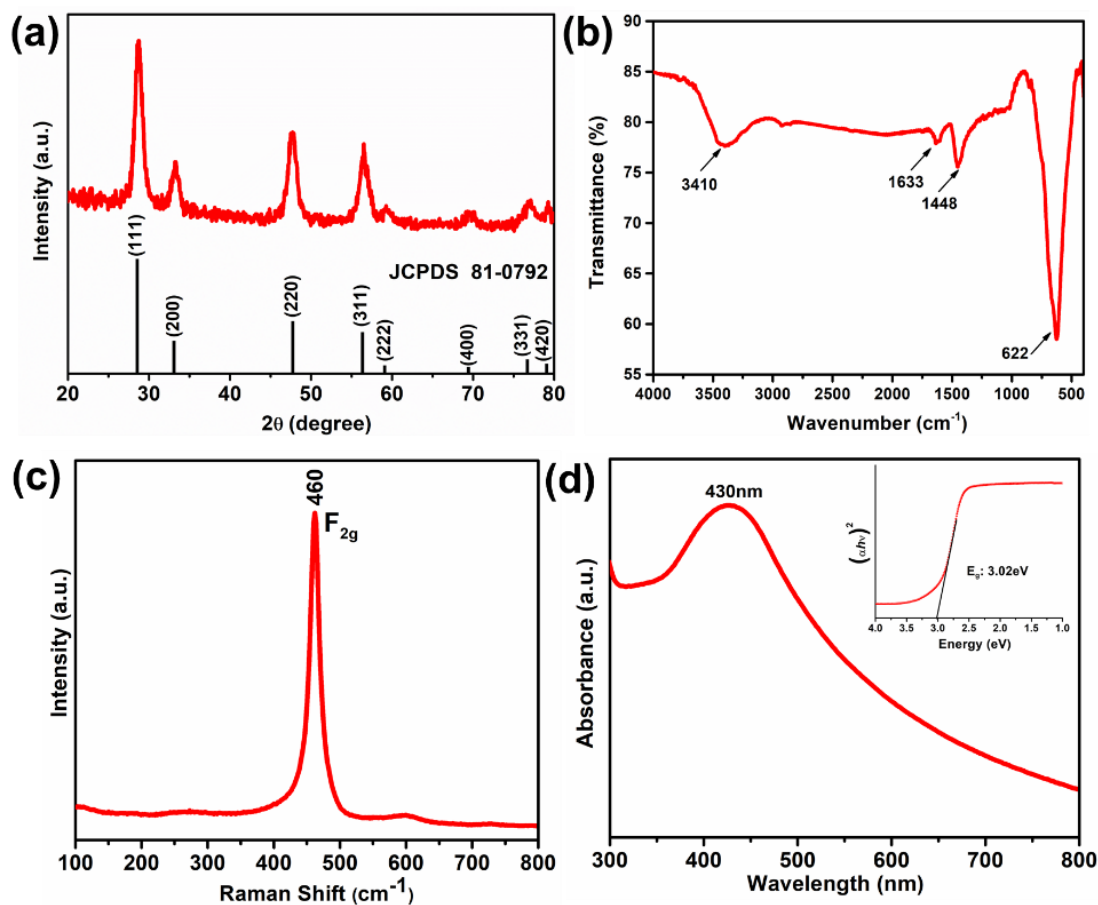


Fig. 2. (a) X-ray diffraction pattern with JCPDS card 81-0792, (b) FTIR, (c) Raman and (d) UV-visible absorption spectrum of CeO₂ nanoparticles (inset: Corresponding Taucs' plot), respectively.

5.3 Scanning Electron and Transmission Electron Microscopic Analysis of CeO₂

The homogeneously distributed dense spherical shape has been observed in the SEM microstructural analysis of synthesized CeO₂, as shown in **Fig. 3a**. **Fig. 3b** and **Fig. 3c** exhibit the bright-field image of the synthesized CeO₂ sample, consisting of a monodisperse particle-like shape having an average size of ~22nm (inset of **Fig. 3c**). Besides, the corresponding HRTEM image reveals different crystalline planes such as (200), (111) and (220) reflection signifying the inter lattice spacing of 0.27, 0.31 and 0.19nm as shown in **Fig. 3d**. The selected area electron diffraction (SAED) pattern indicates that the (111), (200), (220), (311), and (222) planes

correspond to the cubic crystalline phase of CeO₂ nanoparticle as shown in **Fig. 3e**. The EDX result (**Fig. 3f**) confirms that the Ce and O is the only element present in the sample.

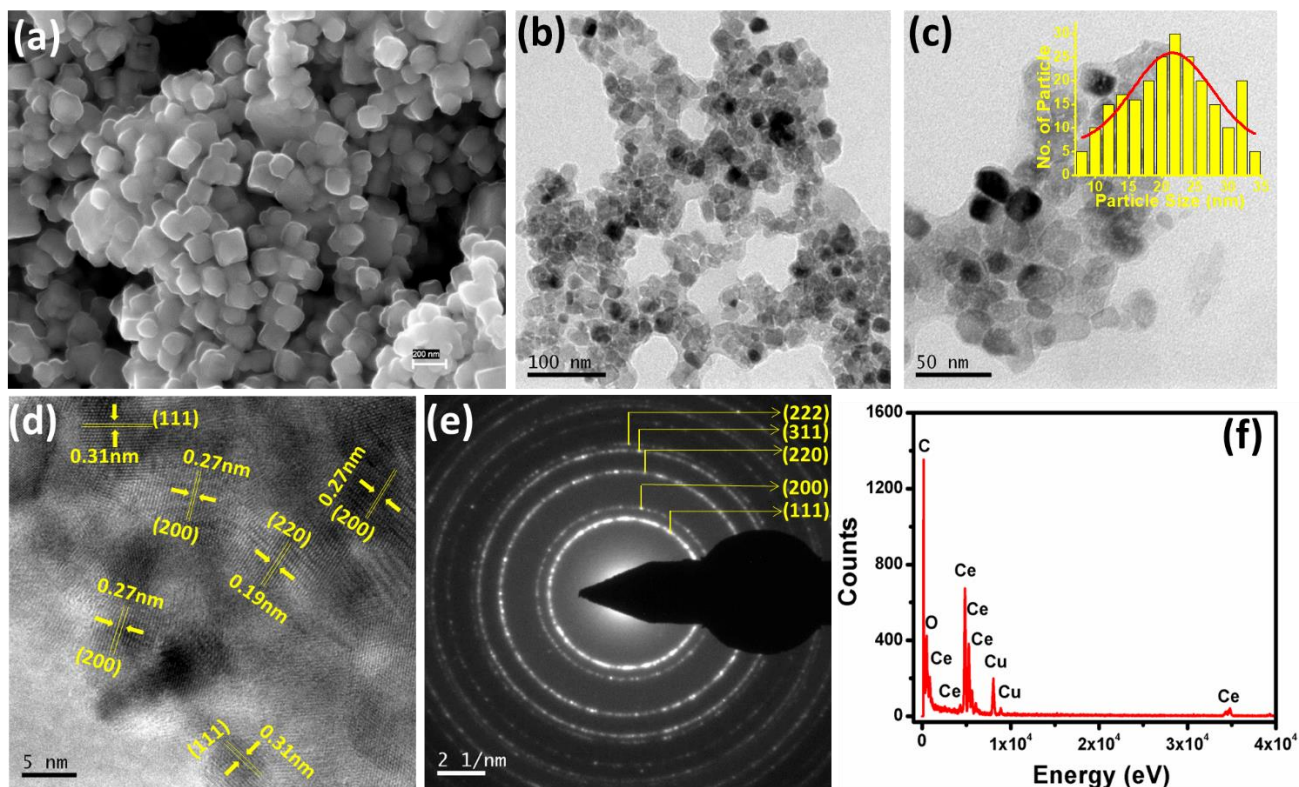


Fig. 3. (a) SEM microstructural image, (b)-(c) TEM bright-field images at different magnification (inset: corresponding histogram of crystalline size distribution), (d) HR-TEM image, (e) SAED pattern and (f) EDX plot of CeO₂ nanoparticles.

5.4 X-ray Photoelectron Spectroscopy Analysis of CeO₂

The XPS survey spectrum of the CeO₂ nanoparticle is shown in **Fig. 4a**, which agrees with the literature reported for CeO₂ [42]. The Ce 3d XPS spectra of the Ce³⁺ ions beside the primary peaks sometimes show the satellites with higher intensity compared to the primary peaks, indicates the co-existence of Ce³⁺ and Ce⁴⁺ bonding states.

The β -ranges are more prominent than the α -ranges for the Ce-3d core level spectrum, as shown in **Fig. 4b**. Besides, α_3 and β_4 signals are responsible for the electronic state of the Ce⁴⁺ ion (3d¹⁰4f⁰). Whereas, Ce³⁺ represents the prominent peaks of α_1 and β_1 indicates the 3d¹⁰4f¹ initial electronic state. Therefore, the CeO₂ consists of both Ce³⁺ and Ce⁴⁺ ions simultaneously, and the fraction of Ce³⁺ ions presence may result in the particle size reduction of the CeO₂ [43]. **Fig. 4c** indicates the core level spectrum of the asymmetric O1s, which consists of two components at 529.89eV (O1 component) and 531.02 eV (O2 component). O²⁻ ions in the Ce-O-Ce metal oxide lattice framework is responsible for the dominant O1 component. In comparison, chemisorbed oxygen in the grain boundaries corresponds to the higher binding side O2 component, which conclusively supports the FTIR data.

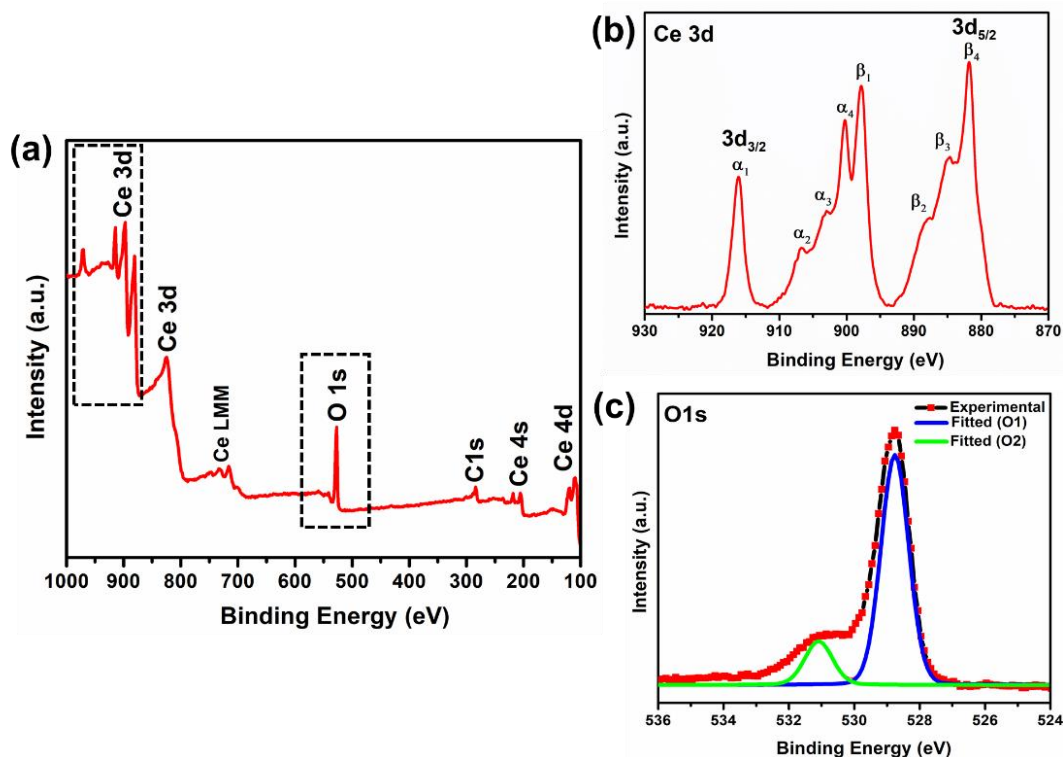


Fig. 4. XPS (a) survey spectrum, core level spectrum of (b) Ce 3d and (c) O1s for CeO₂ nanoparticles.

5.5 Surface Characteristics of CeO₂

Fig. 5a exhibits the room temperature excitation-dependent (300 nm to 345 nm) emission spectra of the CeO₂, resulted in a broad near band emission (NBE) spectrum originating from 4f band of Ce⁴⁺ to the 2p band of O, emanate to a maximum emission peak at 360-370 nm. The intensity of the emission spectrum gets varied on changing the excitation wavelength, originating from band-to-band transition [44]. At the 400-500 nm wavelength zone, the emission multiple weak bands are also appeared due to the oxygen deficiency of the CeO₂ lattice. As a result, the band emission for CeO₂ is relatively stronger compare to its defect-related emission [45, 46]. The BET analysis revealed a surface area of 132.6 m²/g with mesoporous type-IV isotherm characteristics for the CeO₂ nanoparticles, which is higher than the synthesized TiO₂ nanocubes (71.8 m²/g) in **Fig. 4b** [47, 48]. The resultant, more elevated surface area of CeO₂ nanoparticles can effectively lead to absorbed higher dye loading that facilitates the light scattering effect in the DSSC application. Consequently, the BJH average pore diameter improved to 4 nm, ranging from 2-20 nm pore size distribution for the CeO₂ nanoparticles (inset of **Fig. 5b**).

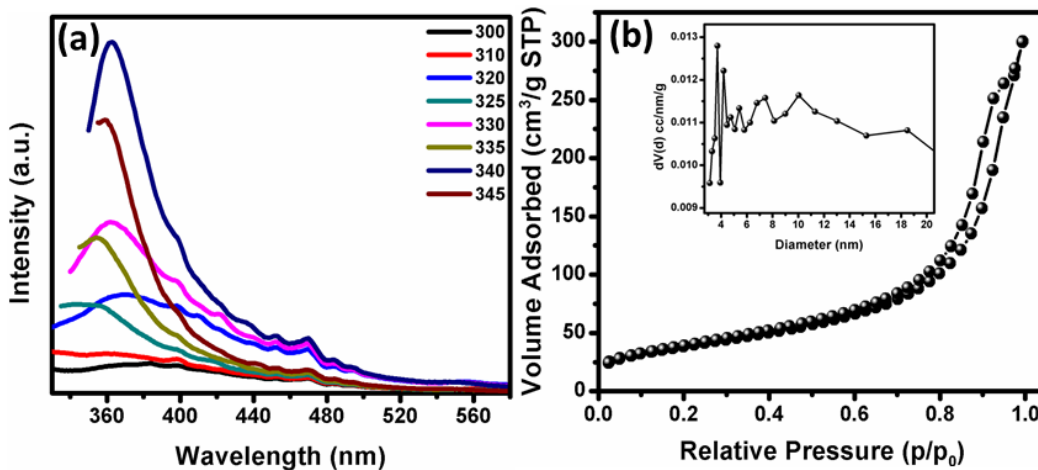


Fig. 5. (a) Excitation wavelength-dependent photoluminescence spectra and (b) BET surface area isotherm of CeO₂ nanoparticles (inset: Corresponding BJH pore size distribution).

5.6 Dye Loading Behavior Study of CeO₂-TiO₂ Film

As shown in **Fig. 6a**, the diffuse reflectance of spectra of the TiO₂ and CeO₂-TiO₂ hybrid photoanode suggests, where CeO₂ employment drastically influences visible light scattering. Therefore, the bandgap of one layer of CeO₂ film is narrower than those of only TiO₂ film in the visible region of the solar spectrum. In particular, one-layer CeO₂ coating exhibits more reflection than the only TiO₂, as shown in **Fig. 6a**. Furthermore, the dye loading amount slightly reduces with one layer coating due to deposition of CeO₂ layer over TiO₂ (**Fig. 6b**). This is probably due to the densely packed top layer of CeO₂ that forge the dye molecules difficult to diffuse efficiently into the TiO₂ porous layers. As a result, even though the thickness of the TiO₂ layer was unchanged, reduced dye-loading was obtained. In addition, nanocrystallite aggregates cause light scattering within the CeO₂-TiO₂ hybrid film. This will further facilitate the travelling distance of light within the device, which finally leads to an improvement in the optical absorption of the device.

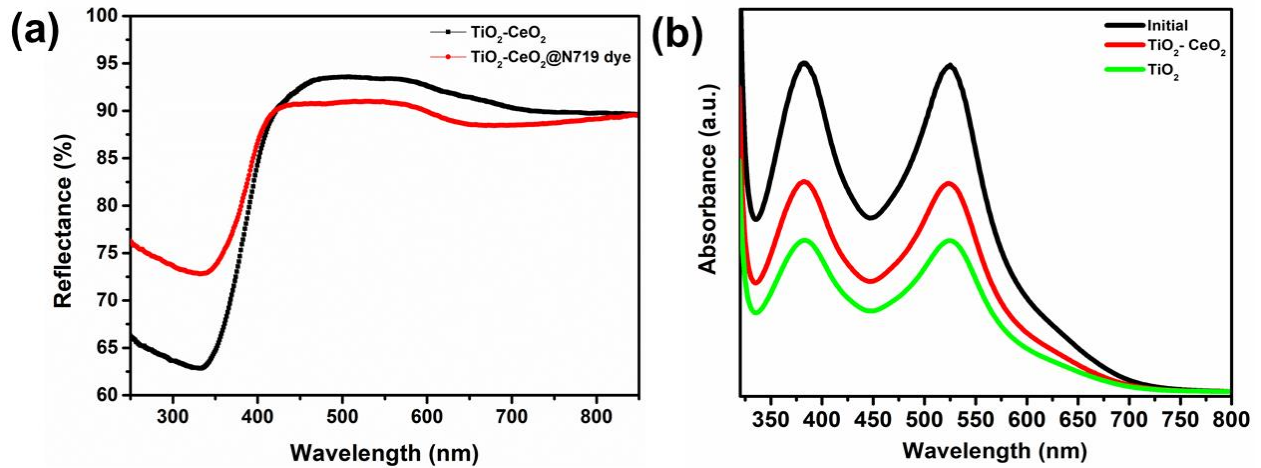


Fig. 6. (a) DR-spectra of TiO_2 nanocube and $\text{CeO}_2\text{-TiO}_2$ hybrid film and (b) UV-vis absorption spectra of N719 dye at its initial state after treatment with TiO_2 nanocubes and $\text{CeO}_2\text{-TiO}_2$ hybrid film.

5.7 Structural Analysis of $\text{CeO}_2\text{-TiO}_2$ Film

To characterize the CeO_2 nanoparticle deposition on TiO_2 nanocube films, the X-ray diffraction studies of the film $\text{TiO}_2\text{-CeO}_2$ (1L) was performed. The appearance of the cubic phase of CeO_2 nanoparticles along with the expected anatase TiO_2 phase confirms the effective deposition of CeO_2 nanoparticles over TiO_2 nanocube (**Fig. 7a**). This further demonstrates the stability of formed CeO_2 even after the sensitization on the photoanode. The cross-sectional microstructure of the same film was further characterized using the FESEM analysis (**Fig. 7b**). The overview of a bilayered photoanode disclosed that the cubic CeO_2 nanoparticle film having an average thickness of $\sim 2 \mu\text{m}$ (for one layer) was evenly coated on the surface of a dense TiO_2 nanocube layer, which consists a thickness of $\sim 5 \mu\text{m}$. It is anticipated that due to consist of a densely packed layer of CeO_2 , the entering of light somewhat restricted and expected to reduce the dye

loading. Therefore, it is a trade-off between layer thickness and diffuse reflectivity of the photoanode to generate high PCE, and considering the fact, one layer of CeO_2 shows the optimum result. The elemental mapping g further confirm the CeO_2 deposition over the TiO_2 throughout the film surface, as illustrated in Fig. 7b.

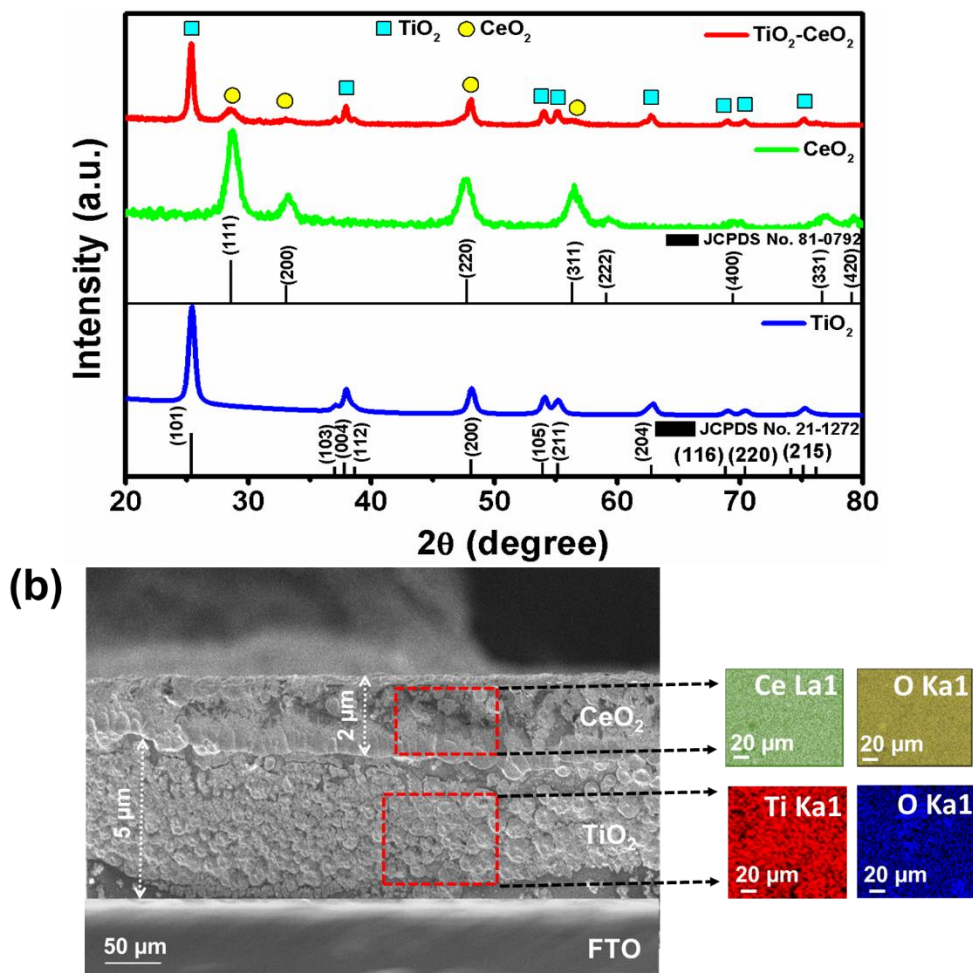


Fig. 7. (a) X-ray diffraction pattern, (b) FESEM cross-sectional view along with the elemental colour mapping of $\text{CeO}_2\text{-TiO}_2$ (1L) in the hybrid film, respectively.

5.8 Photovoltaic Performance of $\text{CeO}_2\text{-TiO}_2$ Photoanode

Fig. 8a revealed the effect of the CeO_2 nanoparticle on its photovoltaic performance using different TiO_2 based photoanodes. Since the nanocrystalline TiO_2 is not sufficiently scattered

visible light, the DSSC with control photoanode shows the power conversion efficiency (PCE) of 6.10% with a current density (J_{sc}) of 14.68 mA/cm² and open-circuit voltage (V_{oc}) 0.75V. The photovoltaic parameters were rapidly enhanced upon adding the first CeO₂ scattering layer (1L) onto the TiO₂ film (STC-1). The STC-1 hybrid electrode, resulting in significant J_{sc} enhancement to 20.62mA cm⁻², V_{oc} to 0.83V and PCE of 8.92% compared to bare TiO₂ nanocube film.

However, with more CeO₂ coating layers, the J_{sc} value was expected to increase more and, therefore, PCE, but the efficiency reduced significantly due to lower J_{sc} . Therefore, the lower PCE of 7.48% was achieved with the two layers (2L) CeO₂ coating as in STC-2 photoanode. To understand the advantage of using the CeO₂ scattering layer over synthesized TiO₂ nanocubes, we have also evaluated a comparative study with the dyesol TiO₂ film, namely DTC-1 and DTC-2, as shown in **Fig. 8a**. An enhancement of ~8% in PCE was achieved using DTC-1 hybrid photoanode with a V_{oc} of 0.75V than only dyesol TiO₂ film, and it is reduced more by ~4% in case of double-layer CeO₂ used (DTC-2). The same efficiency trend follows in DTC hybrid films during the increment of the CeO₂ layer from 1L to 2L as observed for synthesized STC hybrid photoanode. The electrochemical impedance spectroscopy (EIS) measurements were carried out to understand the transport properties at different interfaces in the TiO₂-CeO₂ assembly, shown in **Fig. 8b**. The TiO₂-CeO₂ (ST1) device exhibits an electrochemical charge transfer resistance (R_{CT}) of 953.91 Ω /cm² and a series resistance (R_s) of 84.67 Ω /cm² which is significantly shorter than the only TiO₂ (ST) device. The latter resulted in an R_s value of 98.70 Ω /cm² and a R_{CT} value of 1464.07 Ω /cm². The smallest R_s and R_{CT} value reflects a good bonding between photoanode layers and FTO substrates, promoting the transfer of more electrons/holes from the external circuit, as evident from the enhanced J_{sc} and V_{oc} for the STC1 device. The higher the shunt and

series resistance, the critical impact of parasitic resistance is to reduce the device's FF. However, the higher thickness of the photoanode predominantly resulted in reducing the hybrid device's FF.

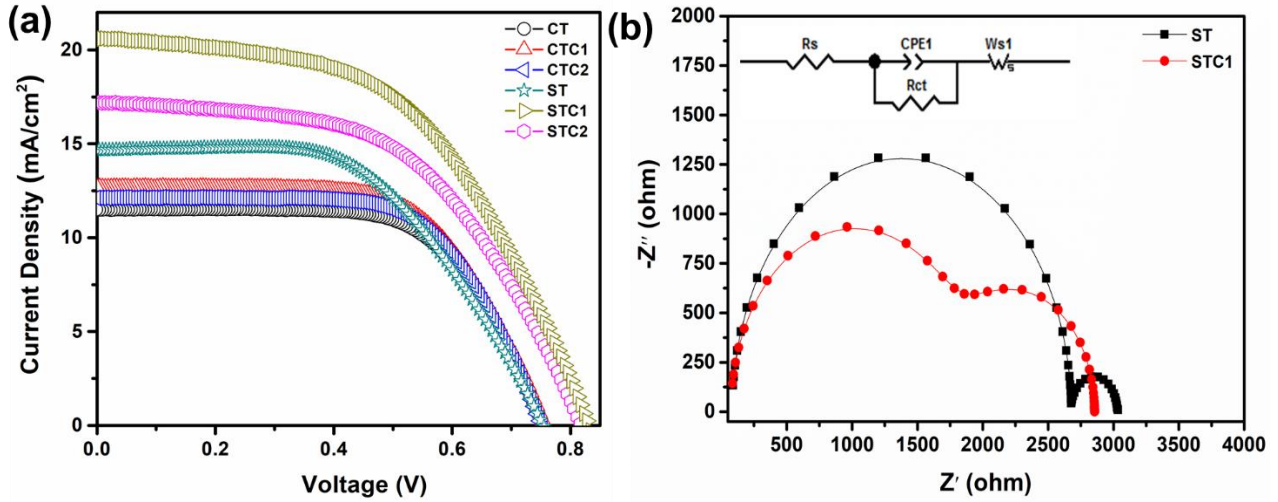


Fig. 8. *J-V* characteristics plot for synthesized only TiO₂ nanocube (ST), only dyesol TiO₂ (CT) and using different scattering layers (1L, 2L) of CeO₂ nanoparticles with the ST and DT hybrid photoanodes for DSSC devices, and (b) corresponding Nyquist plots with the equivalent circuit used for fitting at the inset

Table 1. Comparative photovoltaic parameter study of commercial and synthesized TiO ₂ with synthesized CeO ₂ used as scattering layer for DSSC devices.					
Photoanode	$J_{SC} \pm 0.2$ (mA/cm ²)	V_{OC} (V)	Fill Factor	PCE (%) ± 0.2	PCE Enhancement (%)
ST	14.68	0.75	0.56	6.10	-
STC1	20.62	0.83	0.53	8.92	46.22
STC2	17.19	0.83	0.53	7.48	22.62
CT	11.49	0.75	0.64	5.76	-
CTC1	12.69	0.75	0.63	6.23	8.16
CTC2	12.11	0.75	0.64	6.02	4.15

CT: Commercial TiO₂; ST: Synthesized TiO₂; C: CeO₂; 1,2: Number of layer (s)

It has been observed that a noticeable improvement in J_{SC} and efficiency among the prepared photoanodes with one-layer CeO_2 coating, which provides an optimal and reasonable dual effect of the dye loading and optical scattering effect.

It is speculated that the interfacial contact of large-sized CeO_2 and TiO_2 nanoparticles in the mixture might play an essential role in altering the charge carrier transport. Nevertheless, these experimental pieces of evidence confirmed the beneficial bilayer structure design for efficient light scattering and efficiency improvement of DSSC. An enhancement of ~46% efficiency was observed in the 1L deposition of the CeO_2 scattering layer, whereas it gets reduced to ~22% on a 2L deposit. Though the efficiency has remarkable enhance for both the layer deposition cases than without using the scattering layer. The observed PCE is enormously comparable to the other reports of scattering layer phenomena observed for CeO_2 - TiO_2 bi-layered photoanode in DSSC devices, as shown in **Table 2**. The mirror-like scattering could provide a short pathway for the reflective light and reduce the reflective distance compared to the spherical scattering to reach the dye on the TiO_2 surface. A plausible mechanism of the electron mobility across the hybrid photoanode has been presented in **Fig. 9**. Due to low bandgap and higher surface area, CeO_2 nanoparticles can load more dye compared to TiO_2 as shown in the path 1 and 2 of Fig. 9. However, conduction band (CB) and valance band (VB) position limit the application of CeO_2 as an efficient photoanode utilizing solar energy, even though CeO_2 can absorb a more significant fraction of the solar spectrum than TiO_2 . While the synthesized CeO_2 can effectively participate as a scattering layer which helps to promote more electrons for TiO_2 nanocubes, as shown in path 3 of **Fig. 9**, it is also interesting to note here that the bilayer DSSCs (CeO_2 - TiO_2) had increased V_{OC} relative to the monolayer DSSC (TiO_2) along with J_{SC} and efficiency. The electron and hole diffusion process was further elevated between the dye-oxide cation and redox couple in the

electrolyte due to deceleration of back electron transfer in the CeO₂-TiO₂ hybrid photoanode, further resulting in the device's V_{OC} improvement [49, 50].

Table 2. Comparative Performance of CeO ₂ in a TiO ₂ based DSSC Device				
Description	Type of Use	PCE(%)	PCE Enhancement (%)	Reference
CeO ₂ as scattering layer over TiO ₂	Scattering Layer	8.60%	17.80	30
CeO ₂ as scattering layer over TiO ₂	Scattering Layer	7.95%	45.33	31
P25/Er, YbCeO ₂	Scattering Layer	7.04%	27.94	32
CeO ₂ quantum dots on ZnO nanorods (as sensitizer)	Sensitizer	2.65%	101	49
CeO ₂ -TiO ₂ admixed photoanode with natural dye sensitization	Photoanode	3.50%	-	50
Photoanode CeO ₂ -TiO ₂ sensitized with betacyanin natural dye	Photoanode	2.80%	344	51
CeO ₂ as scattering layer over TiO ₂ -Atomic Layer Deposition	Scattering Layer	9.86%	31.11	53
CeO ₂ :Eu ³⁺	Scattering Layer	8.36%	13.91	54
P25/CeO ₂ : Er, Yb	Scattering Layer	6.66%	15.02	55
CeO ₂ as a light-scattering layer	Scattering Layer	4.55%	46.22	56

over ZnO				
CeO ₂ as scattering layer over TiO ₂	Scattering/Additional Layer	8.92%	46	Current Work

CeO₂ nanoparticle exhibits high surface area, allowing more dye molecule absorption followed by the scattering effect enhancing the device efficiency. However, increasing the thickness of the CeO₂ layer shows PCE decrement also. In addition, CeO₂ owns intrinsic oxygen vacancies that favour electron-hole recombination [51-53]. Therefore, designing CeO₂-TiO₂ tailored aggregates that exhibits light scattering capability would be a viable approach for obtaining highly efficient DSSCs. On the other hand, CeO₂ is also a type of semiconductor, and usually, the bandgap of CeO₂ is narrower than that of TiO₂. Due to the lower bandgap of CeO₂, they are supposed to absorb more light along with the light scattering property than TiO₂ does. Besides, This is more likely that CeO₂ and TiO₂ semiconductors are coupled together, which lead to a narrower bandgap. There is also concern that the stacked scattering particles may impede the interfacial contact between the redox electrolytes and the semiconductor electrodes. Therefore, it is anticipated that a combination of scattering effect and bilayer heterojunction formation could enhance the J_{SC} and V_{OC} of the CeO₂-TiO₂ hybrid photoanodes in the DSSC device.

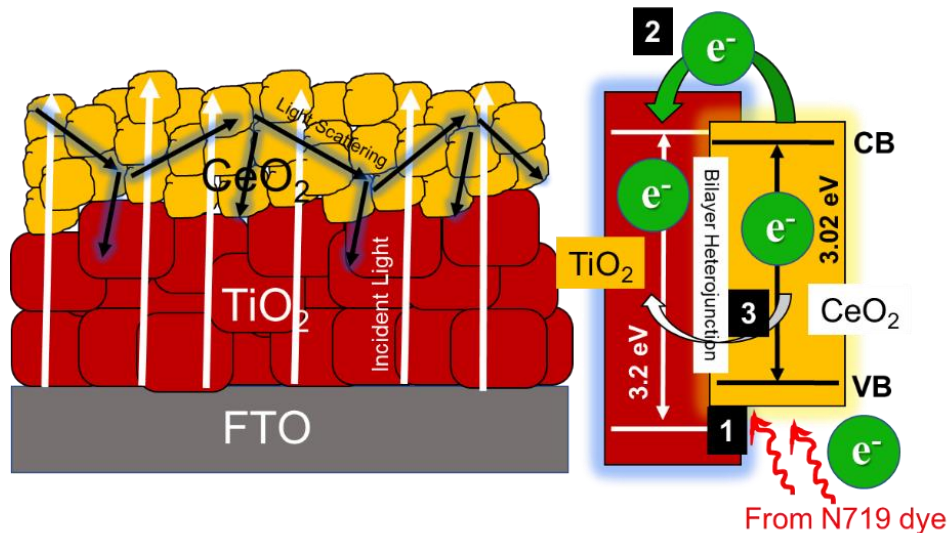


Fig. 9. Schematic illustration of CeO₂-TiO₂ hybrid photoanodes in the DSSC along with their bandgap alignment results in a plausible combined effect of light scattering and heterojunction formation towards enhancing the device's efficiency.

6. Conclusion

The present study provided a new and novel pathway to integrate and test the DSSCs to incorporate with the scattering layer to improve the device's efficiency. Dextran templating synthesis of cubic CeO₂ nanoparticles with an average size of ~22 nm with the visible bandgap ~3.02 eV and a high surface area of 132 m²/g was introduced as the light scattering layers for CeO₂-TiO₂ hybrid photoanodes in DSSCs application. The anatase TiO₂ nanocubes were also synthesized using the hydrothermal method, consisting of an average particle size of 21 nm, having a bandgap of ~3.2 eV, and a specific surface area of ~71 m²/g. The XPS spectrum of CeO₂ revealed the co-existence of Ce³⁺ and Ce⁴⁺ bonding states along with the oxygen deficiency. CeO₂ incorporation can further lead to the effective formation of the CeO₂-TiO₂ heterojunction photoanode that can enhance the dye loading capacity. Finally, compared with the

bare TiO₂ nanocube based control films (6.10%), the DSSCs assembled with ~2 μm CeO₂ top layer exhibited a remarkable ~46% improvement in the power conversion efficiency (8.92%) due to the sparkling light scattering effect of CeO₂ along with the improved V_{OC} of 0.83V resulting from the more robust heterojunction formation. Significant enhancement in the short circuit current and open-circuit voltage predominantly boosts the hybrid device's efficiency.

Furthermore, a comparative study was also performed with the dyesol TiO₂, and there, the efficiency enhancement was found ~8% using the same CeO₂ nanoparticles. Our result indicates that applying CeO₂ on the synthesized TiO₂ nanocubes effectively exhibits higher efficiency enhancement than the commercial TiO₂. It has also been found that the correlation between the light scattering effect of CeO₂, dye loading effect and the heterojunction formation with the TiO₂ requires more depth study that should be addressed in future work.

Acknowledgements

AR acknowledges INSPIRE program, Department of Science and Technology (DST), Government of India for his PhD. A.R. also acknowledges the Newton-Bhabha PhD Program of 2016-2017 jointly funded by DST and the British Council. The authors acknowledge the help rendered by CSIR-Central Glass and Ceramic Research Institute Kolkata 700032, India, to provide material synthesis and characterization facilities.

Notes

The authors declare no competing financial interest.

References

- [1] M. Balat, Solar Technological Progress and Use of Solar Energy in the World, *Energy Sources, Part A Recover. Util. Environ. Eff.* 28 (2006) 979–994. <https://doi.org/10.1080/009083190953409>.
- [2] S. Bhandari, A. Roy, T.K. Mallick, S. Sundaram, Impact of different light induced effect on organic hole-transporting layer in perovskite solar cells, *Mater. Lett.* 268 (2020) 127568. <https://doi.org/https://doi.org/10.1016/j.matlet.2020.127568>.
- [3] L. Tinker, R. Jones-Albertus, Emerging PV technologies: The path to market competitiveness, in: 2016 IEEE 43rd Photovolt. Spec. Conf., 2016: pp. 3471–3474. <https://doi.org/10.1109/PVSC.2016.7750313>.
- [4] R. Xue, J. Zhang, Y. Li, Y. Li, Organic solar cell materials toward commercialization, *Small.* 14 (2018) 1801793. <https://doi.org/https://doi.org/10.1002/sml.201801793>.
- [5] N. Mariotti, M. Bonomo, L. Fagiolari, N. Barbero, C. Gerbaldi, F. Bella, C. Barolo, Recent advances in eco-friendly and cost-effective materials towards sustainable dye-sensitized solar cells, *Green Chem.* 22 (2020) 7168–7218. <https://doi.org/10.1039/D0GC01148G>.
- [6] <<https://www.nrel.gov/pv/cell-efficiency.html>> (2021), Best Research-Cell Efficiency Chart, (n.d.).
- [7] M.A. Deshmukh, S.-J. Park, B.S. Hedau, T.-J. Ha, Recent progress in solar cells based on carbon nanomaterials, *Sol. Energy.* 220 (2021) 953–990. <https://doi.org/https://doi.org/10.1016/j.solener.2021.04.001>.
- [8] S. Zinatloo-Ajabshir, M. Baladi, M. Salavati-Niasari, Enhanced visible-light-driven photocatalytic performance for degradation of organic contaminants using PbWO_4

- nanostructure fabricated by a new, simple and green sonochemical approach, *Ultrason. Sonochem.* 72 (2021) 105420. <https://doi.org/https://doi.org/10.1016/j.ultsonch.2020.105420>.
- [9] H. Safajou, M. Ghanbari, O. Amiri, H. Khojasteh, F. Namvar, S. Zinatloo-Ajabshir, M. Salavati-Niasari, Green synthesis and characterization of RGO/Cu nanocomposites as photocatalytic degradation of organic pollutants in waste-water, *Int. J. Hydrogen Energy.* 46 (2021) 20534–20546. <https://doi.org/https://doi.org/10.1016/j.ijhydene.2021.03.175>.
- [10] V. Mlinar, Engineered nanomaterials for solar energy conversion, *Nanotechnology.* 24 (2013) 42001. <https://doi.org/10.1088/0957-4484/24/4/042001>.
- [11] J. Gong, K. Sumathy, Q. Qiao, Z. Zhou, Review on dye-sensitized solar cells (DSSCs): Advanced techniques and research trends, *Renew. Sustain. Energy Rev.* 68 (2017) 234–246. <https://doi.org/https://doi.org/10.1016/j.rser.2016.09.097>.
- [12] M.S. Sheikh, A. Roy, S. Bhandari, T.K. Mallick, S. Sundaram, T.P. Sinha, Highly conductive double perovskite oxides A_2LuTaO_6 ($A = Ba, Sr, Ca$) as promising photoanode material for dye sensitized solar cells, *Mater. Lett.* 276 (2020) 128220. <https://doi.org/https://doi.org/10.1016/j.matlet.2020.128220>.
- [13] V. Sugathan, E. John, K. Sudhakar, Recent improvements in dye sensitized solar cells: a review, *Renew. Sustain. Energy Rev.* 52 (2015) 54–64. <https://doi.org/https://doi.org/10.1016/j.rser.2015.07.076>.
- [14] K. Sharma, V. Sharma, S.S. Sharma, Dye-Sensitized Solar Cells: fundamentals and current status, *Nanoscale Res. Lett.* 13 (2018) 381. <https://doi.org/10.1186/s11671-018-2760-6>.
- [15] M. Shakeel Ahmad, A.K. Pandey, N. Abd Rahim, Advancements in the development of

- TiO₂ photoanodes and its fabrication methods for dye sensitized solar cell (DSSC) applications. A review, *Renew. Sustain. Energy Rev.* 77 (2017) 89–108. <https://doi.org/https://doi.org/10.1016/j.rser.2017.03.129>.
- [16] H. Mohammadian-Sarcheshmeh, R. Arazi, M. Mazloum-Ardakani, Application of bifunctional photoanode materials in DSSCs: A review, *Renew. Sustain. Energy Rev.* 134 (2020) 110249. <https://doi.org/https://doi.org/10.1016/j.rser.2020.110249>.
- [17] M.-E. Yeoh, K.-Y. Chan, Recent advances in photo-anode for dye-sensitized solar cells: a review, *Int. J. Energy Res.* 41 (2017) 2446–2467. <https://doi.org/https://doi.org/10.1002/er.3764>.
- [18] M. Ge, J. Cai, J. Iocozzia, C. Cao, J. Huang, X. Zhang, J. Shen, S. Wang, S. Zhang, K.-Q. Zhang, Y. Lai, Z. Lin, A review of TiO₂ nanostructured catalysts for sustainable H₂ generation, *Int. J. Hydrogen Energy.* 42 (2017) 8418–8449. <https://doi.org/https://doi.org/10.1016/j.ijhydene.2016.12.052>.
- [19] T. Wan, S. Ramakrishna, Y. Liu, Recent progress in electrospinning TiO₂ nanostructured photo-anode of dye-sensitized solar cells, *J. Appl. Polym. Sci.* 135 (2018) 45649. <https://doi.org/https://doi.org/10.1002/app.45649>.
- [20] A. Roy, S. Mukhopadhyay, P.S. Devi, S. Sundaram, Polyaniline-Layered Rutile TiO₂ Nanorods as Alternative Photoanode in Dye-Sensitized Solar Cells, *ACS Omega.* 4 (2019) 1130–1138. <https://doi.org/10.1021/acsomega.8b02628>.
- [21] P. Ghosh, A. Roy, S. Mukhopadhyay, M. Narjinary, S. Sundaram, S. Sen, P.S. Devi, A New functional composite for photovoltaic and sensor applications, *Adv. Electron. Mater.* 7 (2021) 2000785. <https://doi.org/https://doi.org/10.1002/aelm.202000785>.
- [22] M. Ye, X. Wen, M. Wang, J. Iocozzia, N. Zhang, C. Lin, Z. Lin, Recent advances in dye-

- sensitized solar cells: from photoanodes, sensitizers and electrolytes to counter electrodes, *Mater. Today.* 18 (2015) 155–162. <https://doi.org/https://doi.org/10.1016/j.mattod.2014.09.001>.
- [23] C.D. Lindstrom, X.-Y. Zhu, Photoinduced electron transfer at molecule–metal interfaces, *Chem. Rev.* 106 (2006) 4281–4300. <https://doi.org/10.1021/cr0501689>.
- [24] A. Listorti, B. O'Regan, J.R. Durrant, Electron transfer dynamics in dye-sensitized solar cells, *Chem. Mater.* 23 (2011) 3381–3399. <https://doi.org/10.1021/cm200651e>.
- [25] Z. Zhou, J. Yang, Q. Jiang, W. Li, Y. Luo, Y. Hou, S. Zhou, X. Li, Large improvement of device performance by a synergistic effect of photovoltaics and thermoelectrics, *Nano Energy.* 22 (2016) 120–128. <https://doi.org/https://doi.org/10.1016/j.nanoen.2016.02.018>.
- [26] G. Li, C.P. Richter, R.L. Milot, L. Cai, C.A. Schmuttenmaer, R.H. Crabtree, G.W. Brudvig, V.S. Batista, Synergistic effect between anatase and rutile TiO₂ nanoparticles in dye-sensitized solar cells, *Dalt. Trans.* (2009) 10078–10085. <https://doi.org/10.1039/B908686B>.
- [27] M.N. Mustafa, Y. Sulaiman, Review on the effect of compact layers and light scattering layers on the enhancement of dye-sensitized solar cells, *Sol. Energy.* 215 (2021) 26–43. <https://doi.org/https://doi.org/10.1016/j.solener.2020.12.030>.
- [28] J.-K. Lee, M. Yang, Progress in light harvesting and charge injection of dye-sensitized solar cells, *Mater. Sci. Eng. B.* 176 (2011) 1142–1160. <https://doi.org/https://doi.org/10.1016/j.mseb.2011.06.018>.
- [29] B. V Dias, G.T. Tractz, A. Viomar, G.A.R. Maia, M.T. da Cunha, P.R.P. Rodrigues, Photoelectrochemical Behavior of the cell FTO/TiO₂/CeO₂/N719 obtained from the pechini and precipitation of cerium oxide methods, *J. Electron. Mater.* 47 (2018) 5556–

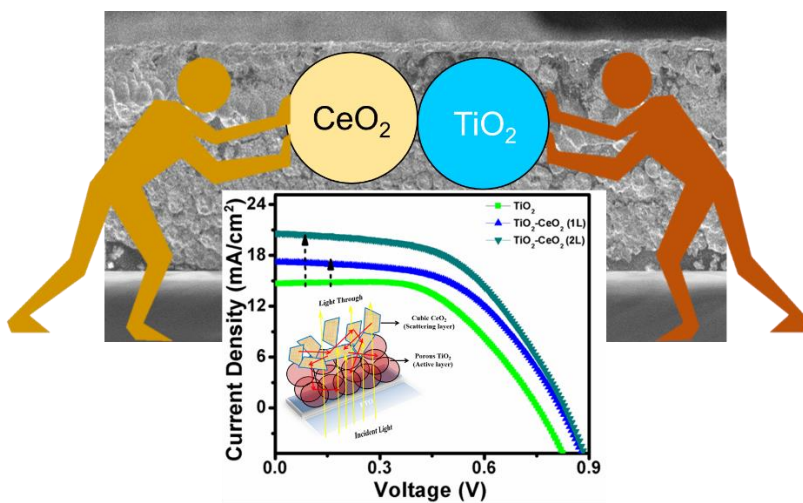
5563. <https://doi.org/10.1007/s11664-018-6465-5>.
- [30] H. Yu, Y. Bai, X. Zong, F. Tang, G.Q.M. Lu, L. Wang, Cubic CeO₂ nanoparticles as mirror-like scattering layers for efficient light harvesting in dye-sensitized solar cells, *Chem. Commun.* 48 (2012) 7386–7388. <https://doi.org/10.1039/C2CC32239K>.
- [31] J. Bai, X. Sun, G. Han, G. Diao, Double-shell CeO₂@TiO₂ hollow spheres composites with enhanced light harvesting and electron transfer in dye-sensitized solar cells, *J. Alloys Compd.* 722 (2017) 864–871. <https://doi.org/https://doi.org/10.1016/j.jallcom.2017.06.102>.
- [32] G. Han, M. Wang, D. Li, J. Bai, G. Diao, Novel upconversion Er, Yb-CeO₂ hollow spheres as scattering layer materials for efficient dye-sensitized solar cells, *Sol. Energy Mater. Sol. Cells.* 160 (2017) 54–59. <https://doi.org/https://doi.org/10.1016/j.solmat.2016.10.021>.
- [33] W. Song, Y. Gong, J. Tian, G. Cao, H. Zhao, C. Sun, Novel Photoanode for dye-sensitized solar cells with enhanced light-harvesting and electron-collection efficiency, *ACS Appl. Mater. Interfaces.* 8 (2016) 13418–13425. <https://doi.org/10.1021/acsami.6b02887>.
- [34] S. Zinatloo-Ajabshir, Z. Salehi, M. Salavati-Niasari, Preparation, characterization and photocatalytic properties of Pr₂Ce₂O₇ nanostructures via a facile procedure, *RSC Adv.* 6 (2016) 107785–107792. <https://doi.org/10.1039/C6RA18470G>.
- [35] S. Zinatloo-Ajabshir, M. Mousavi-Kamazani, Effect of copper on improving the electrochemical storage of hydrogen in CeO₂ nanostructure fabricated by a simple and surfactant-free sonochemical pathway, *Ceram. Int.* 46 (2020) 26548–26556. <https://doi.org/https://doi.org/10.1016/j.ceramint.2020.07.121>.
- [36] T. Montini, M. Melchionna, M. Monai, P. Fornasiero, Fundamentals and catalytic

- applications of CeO₂-based materials, *Chem. Rev.* 116 (2016) 5987–6041.
<https://doi.org/10.1021/acs.chemrev.5b00603>.
- [37] S. Mukhopadhyay, D. Maiti, A. Saha, P.S. Devi, Shape transition of TiO₂ nanocube to nanospindle embedded on reduced graphene oxide with enhanced photocatalytic activity, *Cryst. Growth Des.* 16 (2016) 6922-6932, <https://doi.org/10.1021/acs.cgd.6b01096>.
- [38] A. Roy, P.P. Das, P. Selvaraj, S. Sundaram, P. S. Devi, Template free synthesis of CdSnO₃ micro cuboids for dye sensitized solar cells, *J. Photochem. Photobiol. A* 380 (2019) 111824, <https://doi.org/10.1016/j.jphotochem.2019.04.035>.
- [39] Y. Li, Y. Cai, X. Xing, N. Chen, D. Deng, Y. Wang, Catalytic activity for CO oxidation of Cu-CeO₂ composite nanoparticles synthesized by a hydrothermal method, *Anal. Methods* 7 (2015) 3238-3245, <https://doi.org/10.1039/C5AY00261C>.
- [40] O. P. Moreno, R. G. Pérez, R. P. Merino, M. C. Portillo, G. H. Tellez, E. R. Rosas, M. Z. Tototzintle, CeO₂ nanoparticles growth by chemical bath and its thermal annealing treatment in air atmosphere, *Optik* 148 (2017) 142-150, <https://doi.org/10.1016/j.ijleo.2017.08.133>.
- [41] Y. M. Choi, H. Abernathy, H.-T. Chen, M. C. Lin, M. Liu, Characterization of O₂-CeO₂ interactions using in situ raman spectroscopy and first-principle calculation, *Chem. Phys. Chem.* 7 (2006) 1957-1963, <https://doi.org/10.1002/cphc.200600190>.
- [42] Q. Wang, Y. Li, B. Liu, Q. Dong, G. Xu, L. Zhang, J. Zhang, Novel recyclable dual-heterostructured Fe₃O₄@CeO₂/M (M = Pt, Pd and Pt-Pd) catalysts: synergetic and redox effects for superior catalytic performance, *J. Mater. Chem. A* 2015, 3, 139-147, <https://doi.org/10.1039/C4TA05691D>.
- [43] B. Choudhury, A. Choudhury, Ce³⁺ and oxygen vacancy mediated tuning of structural and

- optical properties of CeO₂ nanoparticles, *Mater. Chem. Phys.* 131 (2012) 666-671, <https://doi.org/10.1016/j.matchemphys.2011.10.032>.
- [44] M.A.M. Khan, W. Khan, M. Ahamed, A. N. Alhazaa, Microstructural properties and enhanced photocatalytic performance of Zn doped CeO₂ nanocrystals. *Sci. Rep.* 7 (2017) 12560, <https://doi.org/10.1038/s41598-017-11074-7>.
- [45] A. Masalov, O. Viagin, P. Maksimchuk, V. Seminco, I. Beshpalova, A. Aslanov, Y. Malyukin, Y. Zorenko, Formation of luminescent centers in CeO₂ nanocrystals, *J. Lumin.* 145 (2014) 61-64, <https://doi.org/10.1016/j.jlumin.2013.07.020>.
- [46] G.H. Jaffari, A. Imran, M. Bah, A. Ali, A. S. Bhatti, U. S. Qurashi, S.I. Shah, Identification and quantification of oxygen vacancies in CeO₂ nanocrystals and their role in formation of F-centers, *App. Surf. Sci.* 396 (2017) 547-553, <https://doi.org/10.1016/j.apsusc.2016.10.193>.
- [47] A. Roy, S. Bhandari, A. Ghosh, S. Sundaram, T. K. Mallick, Incorporating solution-processed mesoporous WO₃ as an interfacial cathode buffer layer for photovoltaic applications, *J. Phys. Chem. A* 124 (2020) 5709-5719, <https://doi.org/10.1021/acs.jpca.0c02912>.
- [48] M. Thommes, K. Kaneko, A.V. Neimark, J. P. Olivier, F. Rodriguez-Reinoso, J. Rouquerol, K. SW Sing, Physisorption of gases with special reference to the evaluation of surface area and pore size distribution (IUPAC Technical Report). *Pure Appl. Chem.* 87 (2015) 1051-1069, <https://doi.org/10.1515/pac-2014-1117>.
- [49] P. Rai, R. Khan, K.-J. Ko, J.-H. Lee, Y.-T. Yu, CeO₂ quantum dot functionalized ZnO nanorods photoanode for DSSC applications, *J. Mater. Sci.: Mater. Electron.* 25 (2014) 2872-2877 (2014), <https://doi.org/10.1007/s10854-014-1954-7>

- [50] R. Upadhyay, M. Tripathi, P. Chawla, A.J. Pandey, Performance of CeO₂-TiO₂-admixed photoelectrode for natural dye-sensitized solar cell, *Solid State Electrochem.* 2014, 18, 1889-1892, <https://doi.org/10.1007/s10008-014-2426-y>.
- [51] M. Tripathi, P. Chawla, CeO₂-TiO₂ photoanode for solid state natural dye-sensitized solar cell, *Ionics* 2015, 21, 541-546, <https://doi.org/10.1007/s11581-014-1172-6>.
- [52] P. Li, Y. Zhou, Z. Zhao, Q. Xu, W. Wang, M. Xiao, Z. Zou, Hexahedron prism-anchored octahedral CeO₂: crystal facet-based homojunction promoting efficient solar fuel synthesis, *J. Am. Chem. Soc.* 137 (2015) 9547-9550, <https://doi.org/10.1021/jacs.5b05926>.
- [53] W. Song, Y. Gong, J. Tian, G. Cao, H. Zhao, C. Sun, Novel photoanode for dye-sensitized solar cells with enhanced light-harvesting and electron-collection efficiency, *ACS Appl. Mater. Interfaces* 21 (2016) 13418-13425, <https://doi.org/10.1021/acsami.6b02887>.
- [54] J. Roh, S. H. Hwang, J. Jang, Dual-functional CeO₂:Eu³⁺ nanocrystals for performance-enhanced dye-sensitized solar cells, *ACS Appl. Mater. Interfaces* 22 (2014) 19825-19832, <https://doi.org/10.1021/am505194k>.
- [55] J. Bai, R. Zhao, G. Han, Z. Lia, G. Diao, Synthesis of 1D up conversion CeO₂:Er, Yb nanofibers via electrospinning and their performance in dye-sensitized solar cells, *RSC Adv.* 5 (2015) 43328-43333, <https://doi.org/10.1039/C5RA06917C>.
- [56] T. Shoji, M. Hagiwara, S. Fujihara, Comparative hydrothermal synthesis of CeO₂ crystals for use in light-scattering layers of dye-sensitized solar cells, *Cryst. Eng. Comm.* 23 (2021) 1415-1422, <https://doi.org/10.1039/D0CE01503B>.

Graphical Abstract Only



CeO₂ nanoparticle exhibits a significant impact as the light scattering layer on top of the anatase TiO₂ nanocube is explored as a hybrid photoanode to enhance efficiency for dye-sensitized solar cells.